The effect of the chemical structure of spinnable pitches on their rheological properties and spinnability and the properties of carbon fibers produced from them

Li Qian[1,2], Zhang Bingfeng[3], Yang Yan[1,2], Zuo Pingping[1], Qin Fangfang[1], Qu Shijie[1,*], Shen Wenzhong[1,*]

(1. *State Key Laboratory of Coal Conversion*, *Institute of Coal Chemistry*, *Chinese Academy of Sciences*, *Taiyuan*, *Shanxi* 030001, *China*;
2. *Center of Materials Science and Optoelectronics Engineering*, *University of Chinese Academy of Sciences*, *Beijing* 100049, *China*;
3. *China Energy Engineering Group Shanxi Electric Power Engineering Co., Ltd*, *Taiyuan*, *Shanxi* 030001, *China*)

Abstract: The structure and composition of a spinnable pitch determine the properties of the carbon fibers produced from it. Spinnable pitches with low and high softening points (L-SP and H-SP) were prepared by air-blowing thermal polymerization of coal tar pitch. The polymerization mechanism, structural composition, properties of the pitch, and the carbon fiber properties were investigated by fluorescence excitation-emission spectroscopy with parallel factor analysis, EPR, ^{13}C-NMR, dynamic shear rheometry, XRD, Raman, etc. L-SP had the lower degree of polymerization, longer alkyl side chains, and a higher proportion of C—O—C groups. At its spinning temperature, the molten L-SP had viscous-dominant rheological characteristics. H-SP had larger polycyclic aromatic hydrocarbon rings, a higher degree of branching, and a higher polarity. The molten H-SP had a high storage and loss moduli, and a rheological behavior with nearly balanced viscous and elastic properties. Although carbon fibers prepared from H-SP had the better physical properties, their inferior rheological properties could lead to melt die swelling, the formation of surface particles and an increased number of irregularities. The superior viscoelasticity of L-SP promoted uniform stretching, maximizing the properties of carbon fibers. This ultimately resulted in similar tensile strengths and moduli of the carbon fibers prepared from the two pitches. The high-quality spinnable pitch had a high aromatic carbon content, a small size of its PAHs, and a low C＝O/O—C＝O content, which ensured viscosity-dominated rheological behavior, thereby reducing die swelling and melt fracture, and the spinning stability and properties of the carbon fibers produced were improved.

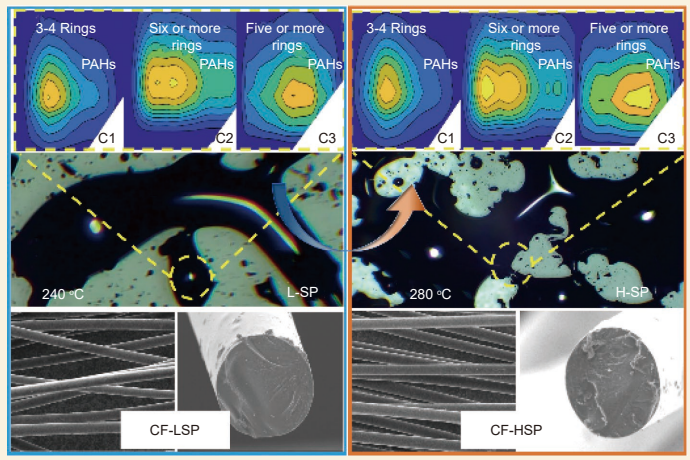

Key words: Chemical composition; Molecular structure; Rheological property; Spinning performance; Pitch-based carbon fibers

1 Introduction

Carbon fiber plays an important role in aerospace, defense, and new energy transportation fields due to its excellent performance[1−2]. In contrast to the superior mechanical performance of polyacrylonitrile-based carbon fiber, pitch-based carbon fiber exhibits typical characteristics of a functional material, particularly in thermal protection and oxidation resistance[3−5]. Various heavy products derived from coal and petroleum, and polycyclic hydrocarbons, are suitable raw materials for preparing pitch-based carbon fiber[6−7]. Among them, coal tar pitch is an excellent precursor due to its high content of poly-

Received: December 19, 2025
Revised: March 05, 2026
Accepted: March 05, 2026

cyclic aromatic hydrocarbons, readily polymerized, cross-linked, graphitized, as well as a high carbon yield[4,8−9]. The quinoline-insoluble components and impurities in coal tar pitch have to be removed, as they affect the rheological properties and spinnability of the spinnable pitch, and ultimately degrade the performance of the resultant carbon fibers[10−11]. It was reported that pitch-based carbon fiber prepared from coal tar pitch (refined by washing oil extraction) showed good mechanical properties[12]. An ideal spinnable pitch should possess a narrow molecular weight distribution, low impurity, heteroatom content, and excellent melt rheological properties[13−14].

Spinnable pitch with suitable softening point, favorable thermal stability, and rheological properties could be obtained by physical or chemical modification[15−18]. Spinnable pitch prepared by the co-carbonization of coal tar pitch with methylnaphthalene or petroleum pitch exhibited a linear molecular structure, which facilitated extrusion from spinnerets and enhanced spinnability[16]. The bromomethylation reaction facilitated the formation of linear molecular structure with methylene cross-linked bridges in spinnable pitch. Moreover, the tensile strength and modulus of resultant carbon fibers were 1210 MPa and 58 GPa[15], respectively. Besides, appropriately raising the spinning temperature could reduce the viscosity of the spinnable pitch, weaken die-swell effect of spinneret, which might enhance the performance of carbon fibers[19].

These results demonstrated that the structure, composition and melt rheology of spinnable pitch determined the performance of resultant pitch-based carbon fiber[20]. However, the performance of pitch-based carbon fiber was usually affected by the combined factors[21]. It was often observed that spinnable pitches with significantly different compositions and structures could exhibit similar carbon fiber performance, presenting a challenge for structure-property prediction. This phenomenon implied a competitive mechanism between structural potential and rheological spinning properties. For instance, while a high degree of polymerization was favorable for structure, poor rheological properties might lead to swelling and fiber breakage during spinning, thereby diminishing structural advantage[19]. Conversely, a precursor with lower polymerization might enhance fiber uniformity during spinning due to superior viscoelasticity and spinnability, thereby improving carbon fiber performance[22]. Therefore, it was crucial to reveal the fundamental cause behind this convergence in carbon fiber performance.

In this work, two types of spinnable pitch were prepared from the same coal tar pitch by air-blowing thermal polymerization at 320 and 370 °C, respectively. The spinnable pitches were further separated into different fractions using column chromatography and solvent extraction. Differences in molecular weight distribution, crosslinking degree, functional groups, as well as the concentration and species of free radicals in the two pitches were systematically analyzed. The melting behavior, key rheological parameters such as modulus and viscoelasticity, as well as spinnability of the spinnable pitches were also investigated. The results showed that pitch-based carbon fibers derived from two structurally distinct spinnable pitches exhibited comparable performance. The underlying reasons for this phenomenon were discussed based on their structural composition and melt rheological behavior. This work provided valuable insights into the factors influencing the performance of pitch-based carbon fibers.

2 Experimental

2.1 Material

Coal tar pitch was provided by Jiexiu Changlong New Material Technology Co. Ltd., China. N-hexane (H), toluene (T), petroleum ether (PE), tetrahydrofuran (THF), and methanol (Me) were purchased from Sinopharm Group, China.

2.2 Preparation and separation of spinnable pitch

Tetrahydrofuran was used for refining coal tar pitch. Using refined pitch as raw material, two spinnable pitches with low and high softening points were prepared by air-blowing thermal polymerization at 320 and 370 °C for 4 h, respectively. The spinnable

pitch prepared by air-blowing polymerization showed fully isotropic pitch (Fig. S1). The refined pitch and spinnable pitches prepared at 320 and 370 °C were labeled as refined coal tar pitch (RCTP), low softening point (L-SP) and high softening point (H-SP), respectively. The basic physical properties of coal tar pitch (CTP) and refined coal tar pitch (RCTP) were listed in Table 1.

Spinnable pitch fraction separation used column chromatography and solvent extraction, respectively. Column chromatography employed 200−300 mesh silica gel as the stationary phase. The silica gel was wetted with n-hexane and wet-packed into the column. The 0.5 g of spinnable pitch was added. The mobile phases were T / PE, T / THF, and Me / THF binary solvent. The eluents were added as follows: 100% H, 20% T / 80% PE, 40% T / 60% PE, 60% T / 40% PE, 80% T / 20% PE, 100% T, 25% THF / 75% T, 50% THF / 50% T, 75% THF / 25% T, 100% THF, and 25% Me / 75% THF, where percentages represented the volume ratios of different solvents. Spinnable pitch was divided into tetrahydrofuran-soluble (THFS) and tetrahydrofuran-insoluble fractions (THFI) by THF as solvent for 24 h using the soxhlet extraction. The THFI fractions were dried in an oven at 75 °C for 3 h. The tetrahydrofuran-soluble and insoluble fractions of the two spinnable pitches were labeled as L-THFS, L-THFI, H-THFS and H-THFI, respectively.

2.3 Preparation of resultant pitch-based carbon fibers

The prepared spinnable pitches were melt-spun at 268 and 305 °C with a winding speed of 400 m/min, respectively. The same stabilization process and carbonization conditions were carried out. The stabilization process used a heating rate of 5 °C/min to 270 °C, followed by 0.5 °C/min to 290 °C and holding for 180 min under air condition. Carbonization treatment was conducted at 1000 °C for 10 min under an inert atmosphere, with a heating rate of 10 °C/min. The resulting pitch-based carbon fibers were denoted as CF-LSP and CF-HSP. The preparation process of the spinnable pitches and the corresponding carbon fibers was illustrated in Scheme 1.

2.4 Characterization

The distribution of polycyclic aromatic hydrocarbons in spinnable pitch eluates was analyzed by three-dimensional excitation-emission matrix (EEM) fluorescence spectroscopy (F-7000 FL) coupled with parallel factor analysis (PARAFAC). EEM-PARAFAC enabled the decomposition of a large number of samples into individual fluorescent components, identifying the unique intensity and peak positions of independent fluorophores. The scanning ranges of excitation wavelength (E_x) and emission wavelength (E_m) were 200–580 nm and 220–600 nm, respectively. PARAFAC analysis of samples was performed using the DOMFluor toolbox in MATLAB R2021b. The molecular weight distributions of the eluates were characterized using an Agilent 1260 instrument from Germany. The functional groups of spinnable pitch, THFS, and THFI fractions were determined by a NICOLET-FT-IR 380 FT-IR spectrometer. Aromaticity (I_{ar})[2,10] and alkyl side chain length (I_{al}) were calculated by $I_{ar} = A_{3150-2990\ cm^{-1}}/A_{2990-2800\ cm^{-1}}$ and $I_{al} = A_{1440\ cm^{-1}}/A_{1375\ cm^{-1}}$, respectively. A Bruker EMX-

Table 1 The basic physical properties of coal tar pitch and refined pitch

Sample	Elemental composition/wt.%					Softening point/°C
	C	H	N	S	O*	
CTP	92.53	4.42	1.00	1.13	0.92	80
RCTP	91.63	5.00	1.19	0.86	1.34	70

Note: O* by difference.

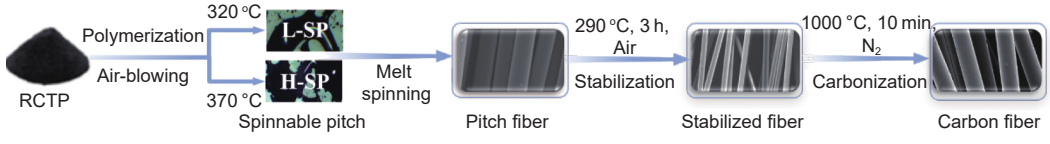

Scheme 1 The preparation process of spinnable pitch and resultant carbon fiber

PLUS 10/12 electron paramagnetic resonance (EPR) spectrometer was used to quantify the concentration and identify the types of free radicals. The elemental compositions of spinnable pitch, THFS and THFI fractions were detected by a vario EL CUBE elemental analyzer. The molecular weight of the spinnable pitch was characterized by matrix-assisted laser desorption/ionization time-of-flight (MALDI-TOF) mass spectrometry using a Bruker Ultraflex. ^{13}C-NMR spectra were recorded on a Bruker Avance III 600 MHz spectrometer. The aromaticity (f_a) of the pitch was calculated based on the integrated areas of the aromatic (90–165 ppm, ppm: 1×10^{-6}) and aliphatic carbon regions (0–90 ppm). XPS was conducted by Kratos AXIS ULTRA DLD (UK) with an Al *K*α X-ray source (1486.6 eV). The XRD (Bruker, Germany) analysis was conducted using Cu-*K*α source radiation (λ = 0.154 06 nm). Raman spectra were tested using a WITec ALPHA 300RAS Raman spectrometer (laser power 3 mW, excitation wavelength 532 nm).

RT600 hot stage with an MM25 microscope was used to observe the melting process of spinnable pitch. The rheological property was characterized by a HAAKE MARS 40 Dynamic Shear Rheometer (DSR). The thermal stability was determined by a TG-DTA 8120 (Rigaku, Japan) with a heating rate of 5 °C/min from room temperature to 800 °C. These tests were conducted in an inert atmosphere.

The tensile strength and Young's modulus of carbon fibers were measured using an ASTM standard D3822-14. The surface morphology of the obtained carbon fiber was acquired by a JSM-7001F SEM.

3 Results and discussion

3.1 Composition of spinnable pitch eluates

L-SP and H-SP were separated by eluting with solvents of different polarities. A three component model was calculated in the eluates of both L-SP and H-SP through EEM-PARAFAC analysis of polycyclic aromatic hydrocarbons (PAHs). C1, C2 and C3 compositions of L-SP and H-SP eluates were shown in Fig. 1a−f. The E_x and E_m loadings for the PARAFAC components were shown in Fig. S2. The range of C1–C3 loadings was listed in Table S1. The similar loadings ranges of L-SP and H-SP eluates were exhibited in C1–C3. The ranges of E_x wavelengths for C1 and C2, and E_m wavelength for C3 in the H-SP eluates were broader. This suggested that a subset of PAHs was common to both L-SP and H-SP, and that the H-SP fraction comprised a greater variety of PAHs[23–25]. The content distribution of three component model in the L-SP and H-SP eluates was shown in Fig. 1g and Fig. 1h, respectively. The difference in the C1−C3 distribution between the L-SP and H-SP eluates indicated that PAHs with the same ring number exhibited distinct abundance profiles in the two spinnable pitches[25–26].

The C1, C2 and C3 loadings from the spinnable pitches were uploaded into OpenFluor with excitation and emission similarity score > 0.97. High similarity to terrestrial humic-like reported was compared to C1[23–24,27–28] and C2[26,29–32], while C3 did not have a comparable model. Further comparison of peaks with databases and standards revealed that C1 likely consisted of 3–4 ring aromatic compounds, which might be alkyl or aryl substituted (e.g., 9,10-Di(1-naphthyl), 1,3,6,8-Tetraphenylpyrene), as well as 3–4 ring coplanar polycyclic aromatic hydrocarbons (e.g., chrysene, pyrene)[23–24]. The C2 was characterized by high molecular weight and aromaticity, which was associated with quinones and PAHs containing six or more coplanar rings, such as benzo[*g, h, i*]perylene[12,26,30,32]. In contrast, C3 exhibited a significant redshift in both excitation and emission wavelengths relative to C1. This suggested the presence of larger ring PAHs, likely with five or more coplanar rings (e.g., perylene)[12]. The C3 content was the lowest (~ 20%), while C1 and C2 accounted for the larger proportion.

The molecular weight distributions of the L-SP and H-SP eluates were shown in Fig. S3, with the average molecular weights listed in Table S2. In general, the molecular weight of the eluates increased with eluent's polarity. Specifically, as the eluent polarity increased from n-hexane to 100% toluene, the mass-average molecular weight (M_w) increased from 298.2 g/mol to 725.6 g/mol for L-SP, and from

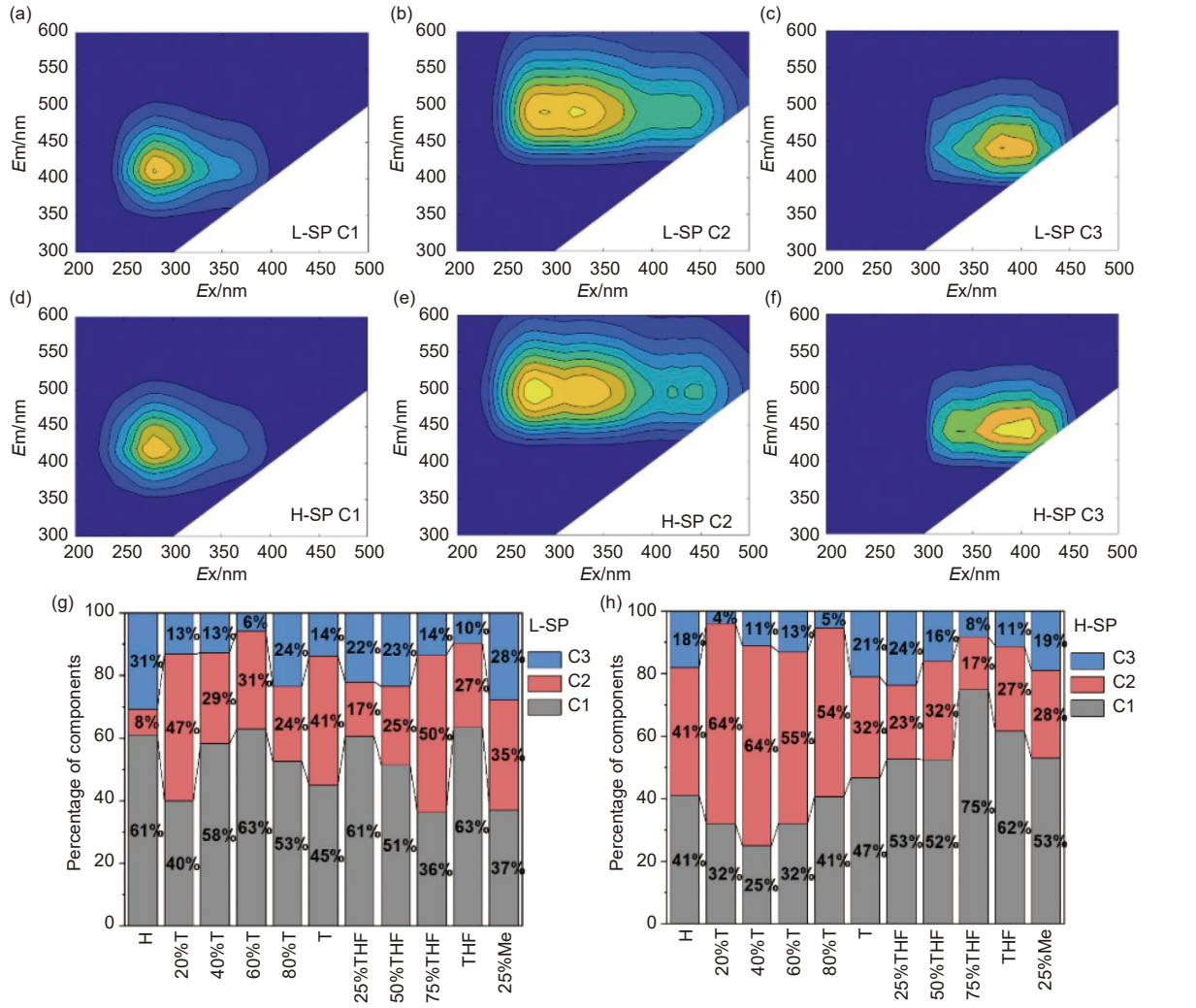

Fig. 1 PARAFAC model of the three compounds in L-SP eluates and H-SP eluates, (a–c) C1, C2 and C3 of L-SP eluates, (d–f) C1, C2 and C3 of H-SP eluates, and the three compounds distribution of (g) L-SP eluates and (h) H-SP eluates

317.7 g/mol to 483.3 g/mol for H-SP. With the eluent further changed to 100% THF, the M_w increased to 844.7 g/mol (L-SP) and 706.4 g/mol (H-SP), respectively. The z-average molecular weight (M_z) exhibited an even more pronounced increase, with L-SP reaching 1052.0 g/mol in the 100% THF eluate, while H-SP reached 898.5 g/mol in the 25% Me / 75% THF eluate.

H-SP exhibited a near-monotonic increase in average molecular weight with polarity, a trend likely attributed to the concurrent rise in its C1 content. In contrast, L-SP showed more complex fluctuations, particularly with highly polar solvents. Notably, H-SP had higher molecular weights than L-SP when eluted with weakly polar solvents (higher in n-hexane and petroleum ether), whereas the trend reversed under strong polar solvents (100% toluene, THF), with L-SP attaining higher values. The particularly significant molecular weight increase for H-SP in methanol-containing eluates suggested a higher hydrogen-bonding content and potentially greater polarity[33].

3.2 Structural and compositional evolution of spinnable pitch

The molecular weight distribution of RCTP, L-SP and H-SP was shown in Fig. 2a. The molecular weight distribution range of RCTP was primarily 200–600 Da. The increase and broadening of molecular weight were observed after air-blowing polymerization reaction, with a significant shift toward the high m/z region. The molecular weight distribution range of L-SP was 200–1200 Da. H-SP exhibited a broader distribution range with the peak center at 1100 Da, in-

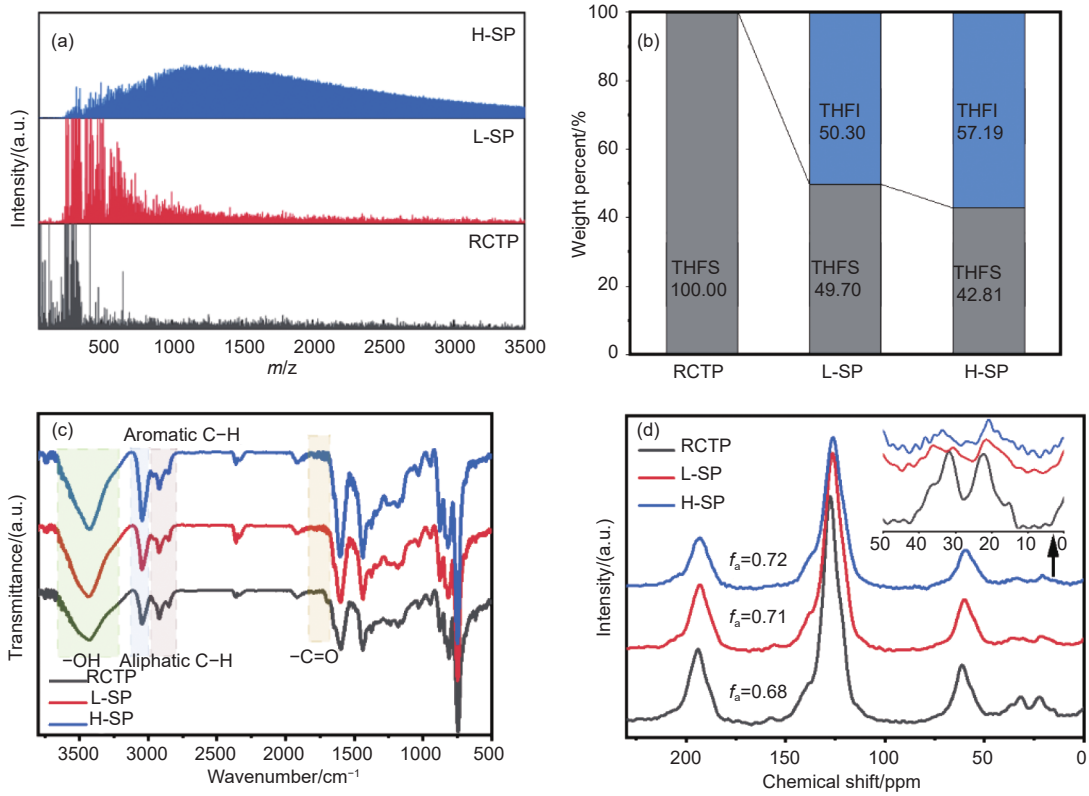

Fig. 2　(a) Molecular weight, (b) extraction fraction content, (c) FT-IR spectra, and (d) ^{13}C-NMR spectra of RCTP, L-SP and H-SP (ppm: 1×10^{-6})

dicating macromolecular composition substantially increased. The number average molecular weight increased from 864.86 Da (RCTP) to 1042.44 Da (L-SP) and 1662.84 Da (H-SP), respectively.

L-SP and H-SP were divided into tetrahydrofuran-soluble fractions (L-THFS and H-THFS) and tetrahydrofuran-insoluble fractions (L-THFI and H-THFI) by THF extraction (Fig. 2b). The weight contents of L-THFS and L-THFI in L-SP were 49.70% and 50.30%, respectively. The contents of H-THFS and H-THFI in H-SP were 42.81% and 57.19% (mass fraction). H-SP showed a lower THFS fraction and a higher THFI fraction than L-SP, which might be the result of more macromolecular content and higher molecular polymerization degree[34].

FT-IR spectra of RCTP, L-SP and H-SP were presented in Fig. 2c. RCTP and spinnable pitch exhibited prominent hydroxyl (3500 cm^{-1}) absorption peaks. The intensity of the carbonyl peak (1700 cm^{-1}) increased after thermal polymerization. The carbonyl peak in H-SP showed the strongest intensity, suggesting the content was the highest. The intensity of the aromatic ring C—H (3050 cm^{-1}) absorption peak gradually increased, whereas the aromatic C—H (2920, 2850 cm^{-1}) absorption peak gradually decreased. The aromaticity index (I_{ar}) of RCTP, L-SP and H-SP was 0.45, 0.54 and 0.55, respectively. The aromaticity increased significantly from RCTP to spinnable pitch. The aromaticity of H-SP was slightly higher than that of L-SP. Peaks near 1440 and 1375 cm^{-1} belonged to methylene and methyl C—H stretching vibrations, respectively. The aliphatic chain lengths (I_{al}) of RCTP, L-SP and H-SP were 2.73, 2.38 and 2.17, respectively, which indicated a shorter aliphatic chains after thermal polymerization[12]. The L-THFS and H-THFS fractions exhibited notably stronger absorption intensities at 1700 cm^{-1}, indicating a higher carbonyl content within the THFS fractions, with the H-THFS fraction showing the highest value (Fig. S4). These results indicated that H-SP possessed a higher carbonyl content, comparable aromaticity, and shorter aliphatic chains compared with L-SP. The increased polar groups and shorter aliphatic chains in H-SP might lead to stronger intermolecular forces and poorer fluidity[21−22].

Fig. 2d showed the ^{13}C-NMR spectra of RCTP,

L-SP, and H-SP. The aromaticity (f_a) increased from 0.68 (RCTP) to 0.71 (L-SP) and 0.72 (H-SP), which indicated that the aromatic carbon content increased. The C_{al3} content increased, C_{al2} decreased, C_{al3}/C_{al2} ratio increased from 0.87 (RCTP) to 0.99 (L-SP) and further to 1.24 (H-SP) (Table 2), suggesting a shortening of the aliphatic chains. L-SP retained a considerable proportion of $-CH_2$ groups, whereas H-SP exhibited a substantial loss of $-CH_2$, confirming its shorter aliphatic chains. These findings were consistent with the FT-IR results. Moreover, the peak intensity at 30–40 ppm significantly decreased. It could be attributed to the oxidation of benzylic $-CH_2$ groups[35]. Concurrently, the $C_{al1}/(C_{al3}+C_{al2})$ ratio increased from 0.13 in RCTP to 0.15 in L-SP and 0.16 in H-SP, suggesting an increase in structural cross-linking and branching sites.

A significant upfield shift in the aromatic carbon peak was observed, from 127.5 ppm (RCTP) to 126.4 ppm (L-SP) and 126.2 ppm (H-SP). This indicated that electron density of the aromatic carbons increased, molecular conjugation enhanced, polycyclic aromatic hydrocarbons size enlarged. The content of C_{ar}^{H} decreased while that of C_{ar}^{C} increased[15] (Table 3), which indicated the molecules underwent polymerization. Concurrently, the slight decrease in C_{ar}^{S} suggested the conversion of some alkyl-substituted carbons into bridgehead types. This process was consistent with the noted upfield chemical shift. The content of C_{ar}^{O} also increased, pointing to progressive oxidation. H-SP demonstrated a more pronounced transformation than L-SP, exhibiting a significant reduction in C_{ar}^{H} and a larger increase in C_{ar}^{C}. This comparative result indicated that H-SP underwent a higher degree of condensation and developed more extensive bridged aromatic structures[8].

The elemental compositions of RCTP, spinnable pitch, THFS and THFI fractions were listed in Table S3. Oxygen likely participated in cross-linking and dehydrogenation polymerization reactions during the air-blowing thermal polymerization process[37–38]. This led to a decrease in the H/C ratio from 0.65 (RCTP) to 0.57 (L-SP) and further to 0.53 (H-SP), accompanied by an overall increase in oxygen content. Concurrently, the content of nitrogen and sulfur slightly decreased. Notably, H-SP exhibited a lower oxygen content than that of L-SP. It might be attributed to the decomposition of peroxide groups and the potential loss of oxygen and hydrogen released as water[39]. Furthermore, THFS fractions showed higher H/C ratio compared with spinnable pitches, this was likely a result of their lower aromatic content and higher saturated aliphatic hydrocarbon content[40]. The THFS fractions contained higher concentrations of sulfur, oxygen, and hydrogen than that of THFI fractions. The lower H/C ratio in the THFI fractions indicated more complex structures and higher polycyclic aromatic hydrocarbons content[41].

XPS analysis was employed to investigate the evolution of surface functional groups (Fig. S5). The

Table 2 The distribution of aliphatic carbon of RCTP, L-SP and H-SP

Sample	Aliphatic carbon distribution/%			C_{al3}/C_{al2}	$C_{al1}/(C_{al3}+C_{al2})$
	C_{al3}	C_{al2}	C_{al1}		
RCTP	41.15	47.51	11.34	0.87	0.13
L-SP	43.09	43.73	13.18	0.99	0.15
H-SP	47.96	38.58	13.46	1.24	0.16

Note: C_{al1}, C–H carbons, 36–45 ppm; C_{al2}, methylene/naphthenic bridge carbons, 25–36 ppm; and C_{al3}, terminal methyl carbons, 0–25 ppm[4,8,36] (ppm: 1×10^{-6}).

Table 3 The distribution of aromatic carbon of RCTP, L-SP and H-SP

Sample	Aromatic carbon distribution/%			
	C_{ar}^{H}	C_{ar}^{C}	C_{ar}^{S}	C_{ar}^{O}
RCTP	61.97	26.14	9.51	2.38
L-SP	59.43	29.10	9.05	2.42
H-SP	58.85	29.86	8.65	2.65

Note: C_{ar}^{H}, protonated aromatic carbons, 90–129 ppm; C_{ar}^{C}, aromatic bridgehead carbons, 129–137 ppm; C_{ar}^{S}, alkyl-substituted aromatic carbons, 137–148 ppm; and C_{ar}^{O}, oxygen-substituted aromatic carbons, 148–164 ppm.

peak-fitted data was listed in Table S4. The deconvoluted C 1s spectra of RCTP, L-SP and H-SP were presented in Fig. 3a-c. The content of C–C/C=C bonds decreased, while the combined content of oxygen-containing functional groups (C—O, C=O, O—C=O) increased. For L-SP, the C—C/C=C content decreased from 72.30% to 63.88%, accompanied by an increase in C—O content from 13.69% to 17.06%. In contrast, H-SP showed a markedly different profile. It exhibited a smaller reduction in C—C/C=C content (69.40%), and the increase in oxygen-containing groups was minimal. This was consistent with the lower oxygen content measured for H-SP compared with L-SP. H-SP had a higher thermal polymerization temperature, potentially enabling decarboxylation, decarbonylation, and dehydration[42–43]. The oxygen-containing bond cleavage and aromatic ring condensation might occur. This shift was consistent with the significant increase in bridgehead carbons (C_{ar}^{C}) and the decrease in oxygen content, indicating deeper condensation and the formation of more extensively bridged aromatic structures.

The distribution of different oxygen-containing functional groups in RCTP, L-SP and H-SP was presented in Fig. 3d-f. After thermal polymerization, the contents of O—C=O and C=O increased while C—O decreased. The gradual transformation of C—O bonds into O—C=O and C=O bonds occurred, the molecular crosslinking degree enhanced[44]. For L-SP, the content of C—O bonds remained higher than that of C=O and O—C=O bonds, with O—C=O content increasing from 28.32% to 38.00%. As for H-SP, C=O and O–C=O bonds surpassed C–O bonds. The significant increase in O—C=O content (45.36%) was observed, and C=O content increased from 4.43% (RCTP) to 7.01%. This further indicated that over-oxidation might occur in H-SP, resulting in increased molecular crosslinking and polarity.

EPR spectra of RCTP, spinnable pitches were shown in Fig. 4a. The g-value, free radical concentration and linewidth of different samples were listed in Table S5. The free radical concentration increased from 1.23×10^{18} spins/g (RCTP) to 6.30×10^{18} spins/g (L-SP) and 9.44×10^{18} spins/g (H-SP). The ratio of THFI/THFS radical concentration increased from 33 (L-SP) to 206 (H-SP), demonstrating that active radicals were preferentially trapped within the developing insoluble network during high-temperature air-blowing polymerization. EPR spectral parameters revealed distinct radical types.

The EPR spectra of RCTP, L-SP and H-SP were fitted to one Gaussian and 3 Lorentzian lines[45–47] (Fig. 4b-d). Based on g-values, these components were assigned as follows: Gaussian – simple aromatic

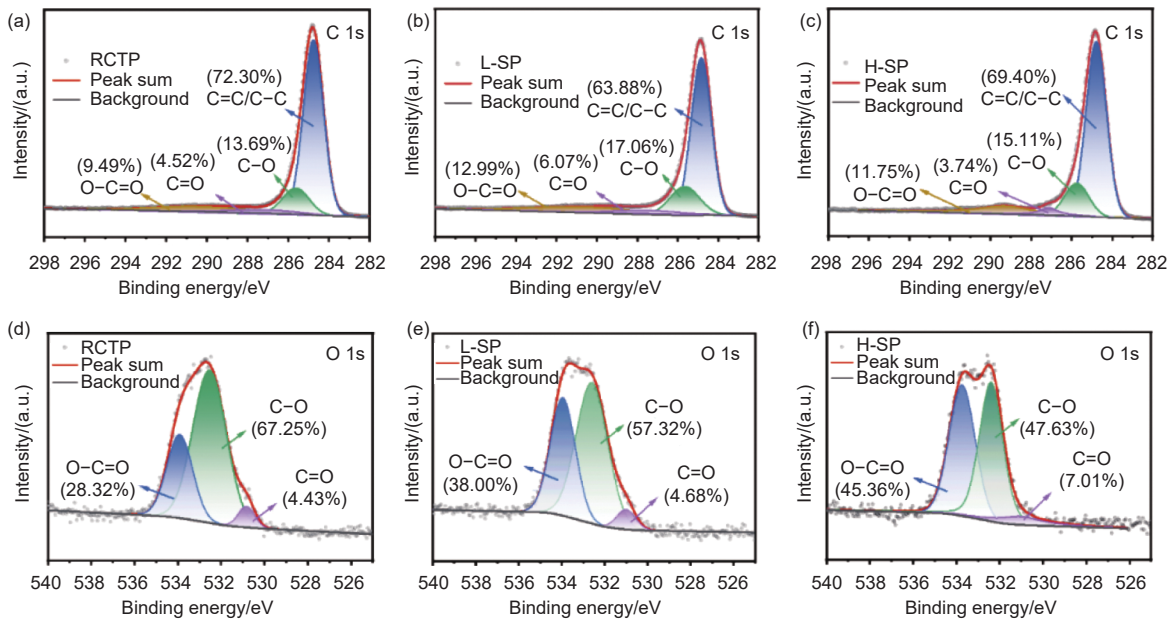

Fig. 3 XPS spectra of RCTP, L-SP and H-SP. C 1s of (a) RCTP, (b) L-SP and (c) H-SP. O 1s of (d) RCTP, (e) L-SP and (f) H-SP

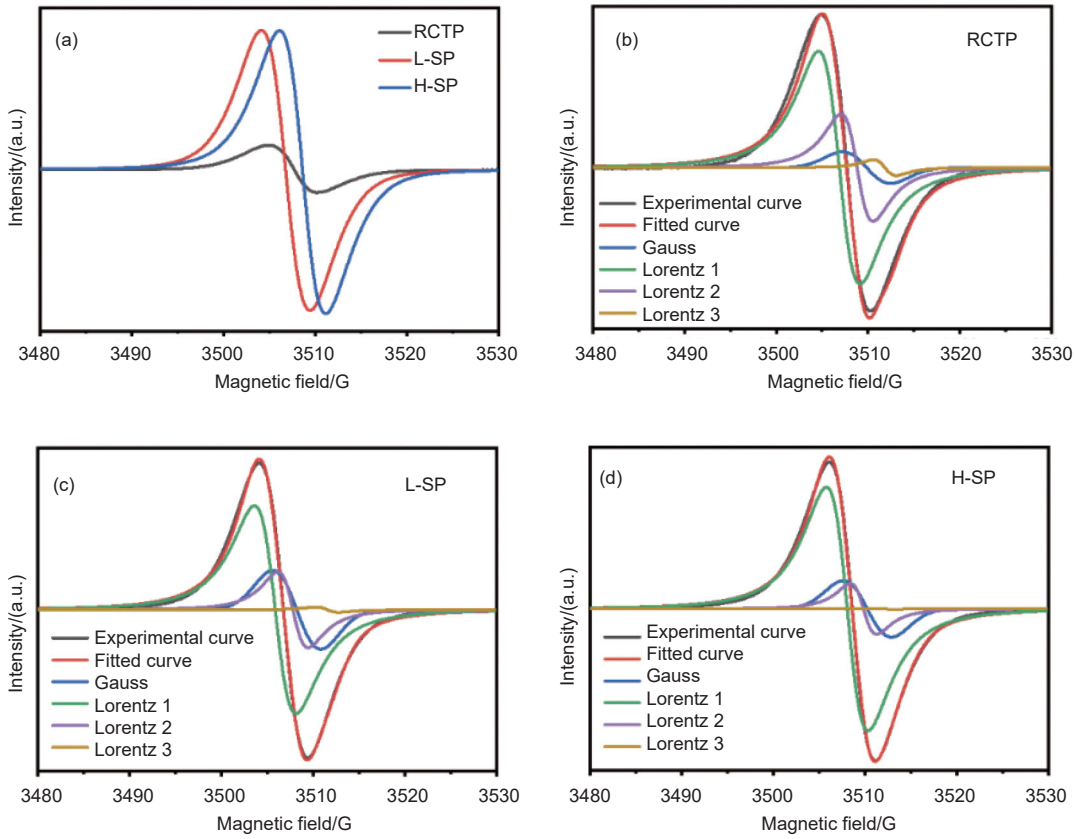

Fig. 4 (a) EPR spectra of RCTP, L-SP, and H-SP. The fitted figure of EPR spectra of (b) RCTP, (c) L-SP, and (d) H-SP

radicals; L1 – π-type oxygen radicals (e.g., quinones); L2 – aliphatic hydrocarbon radicals hybridized with aromatic hydrocarbons; L3 – σ-type oxygen radicals. Fitting results were listed in Table S6. Quantitative data (Table 4) revealed distinct trends. H-SP had the highest total radical concentration. The simple aromatic radical concentration rose from 8.12×10^{16} spins/g (RCTP) to 1.11×10^{18} spins/g (L-SP) and 1.21×10^{18} spins/g (H-SP), confirming aromatization[8]. The π-type oxygen radicals (L1) were dominant. Their concentration increased to 7.28×10^{18} spins/g in H-SP, constituting 77.14% of its radical content, which confirmed quinone formation[43] and aligned with EEM-PARAFAC results. The high abundance of these stable, delocalized radicals in H-SP favored condensation bridging reactions. Conversely, aliphatic-type radicals (L2) decreased, consistent with consumption via benzylic oxidation leading to side-chain cleavage[12,35,42]. The unstable σ-type radicals (L3) were negligible. In summary, high-temperature processing (H-SP) consumed aliphatic structures while generating more stable π-type oxygen radicals, thereby promoting the progress of condensation reactions and achieving a deeper degree of polymerization.

The g-value decrease was attributed to the increased aromatic hydrocarbon radical content[47]. H-SP showed a slightly higher g-value than L-SP, consistent with its higher π-type oxygen radical content. This trend aligned with the overall structural evolution toward higher aromaticity, C=O content, and cross-linking during air-blowing thermal polymerization. H-SP represented a deeper level of reaction, character-

Table 4 The radical concentrations and contents of different types in RCTP, L-SP and H-SP

Sample	Gaussian line		Lorentzian line 1		Lorentzian line 2		Lorentzian line 3	
	Concentration /(spins/g)	Percentage/%	Concentration /(spins/g)	Percentage/%	Concentration /(spins/g)	Percentage/%	Concentration /(spins/g)	Percentage/%
RCTP	8.12×10^{16}	6.60	8.29×10^{17}	67.39	2.91×10^{17}	23.66	2.88×10^{16}	2.34
L-SP	1.11×10^{18}	17.64	4.07×10^{18}	64.74	1.05×10^{18}	16.79	5.20×10^{16}	0.83
H-SP	1.21×10^{18}	12.85	7.28×10^{18}	77.14	9.34×10^{17}	9.89	1.08×10^{16}	0.11

ized by more quinones and C=O bonds, larger aromatic size, shorter alkyl chains, stronger polarity, and a deeper cross-linking degree. The corresponding reaction pathways were shown in Fig. 5.

3.3 The properties of spinnable pitch and performance of carbon fibers

The thermal behaviors of the spinnable pitch and its extraction fractions were investigated by a thermogravimetric analysis (TG). As shown in Fig. 6a, the total weight loss decreased from 78.77% (RCTP) to 51.57% (L-SP) and 44.17% (H-SP). A significant weight loss occurred at 280–580 °C was primarily due to the volatilization of small molecules released through condensation, dealkylation, and dehydrogenation reactions[15,18,22]. The derivative thermogravimetry (DTG) curves were shown in Fig. S7a. The maximum weight loss rate for RCTP occurred at approximately 300 °C, while for L-SP and H-SP, it increased to 400 and 420 °C, respectively. H-SP exhibited the highest temperature for the maximum weight loss rate, which could be attributed to its higher degree of polymerization and cross-linking[16]. The THFI fraction, characterized by a larger molecular weight and a higher degree of condensation, showed a higher carbon yield, with weight loss rates of 18.01% for H-THFI and 22.70% for L-THFI (Fig. 6b). The weight loss rates of both the soluble and insoluble fractions in L-SP were higher than those in H-SP. Consequently, H-SP demonstrated a higher carbon yield. However, excessive polymerization of the soluble fractions might increase the viscosity and elasticity of the pitch during melting[48], which was unfavorable for the spinning process.

The melting behavior of the spinnable pitches was examined. The melting ranges of L-SP and H-SP were 200–240 °C and 240–280 °C, respectively, indicating a higher softening point for H-SP. The corresponding melting micrographs were presented in Fig. 7. Complete melting occurred at 240 °C for L-SP and 280 °C for H-SP, representing the optimal molten states for spinning. After cooling to room temperature, H-SP became brittle and prone to fracture. This brit-

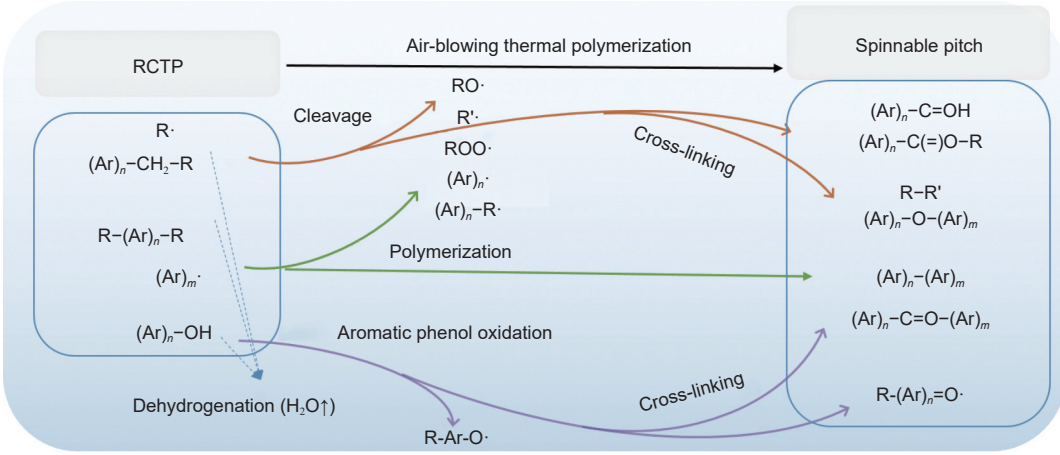

Fig. 5 Possible reaction pathways in air-blowing thermal polymerization of RCTP

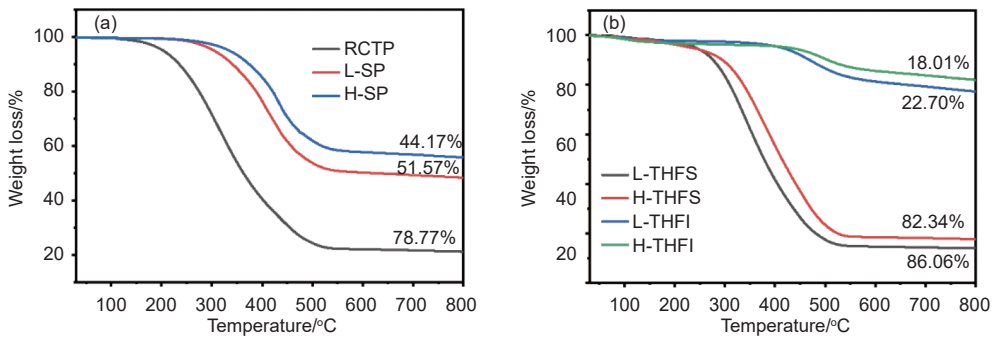

Fig. 6 TG curves of (a) spinnable pitch and (b) extraction fractions

tleness likely impeded elongation during the spinning process, thereby increasing the risk of fiber breakage.

L-SP and H-SP were melt-spun at 268 and 305 °C, under spinning pressures of 1.0 and 1.2 MPa, respectively. L-SP exhibited superior spinnability, with no fiber breakage observed throughout continuous spinning at 400 m/min. In contrast, H-SP could be spun continuously for only up to 30 min at the same speed. The need for higher spinning temperature and pressure, together with poorer spinning stability, was attributed to the rheological characteristics of H-SP.

The variations of complex viscosity ($|\eta|$), complex modulus (G), storage modulus (G'), and loss modulus (G'') of spinnable pitches with temperature were shown in Fig. 8. The G' reflected the elastic property of the spinning pitch. At a constant angular frequency, the fluidity of spinning pitch improved as temperature increased, while its elasticity and storage modulus decreased[49]. The G'' represented the viscous property, corresponding to the energy dissipated as heat due to internal friction during deformation; it was proportional to viscosity[50]. As temperature increased, the shear resistance weakened, causing the loss modulus to gradually decrease. During heating, the spinnable pitch gradually transitioned from elastic-dominant to viscous-dominant behavior, with both modulus and viscosity decreasing, exhibiting shear-thinning (pseudoplastic) flow characteristics.

The ratio of G'' to G' (tanδ) indicated whether elastic or viscous behavior dominated under given conditions[49−50]. At the spinning temperature, the tanδ of H-SP was approximately 1, signifying a high-modulus melt with a near-equilibrium between viscous and elastic properties. In contrast, L-SP exhibited much lower viscosity and storage modulus, with a tanδ of 4.8, indicating a viscous-dominant melt that

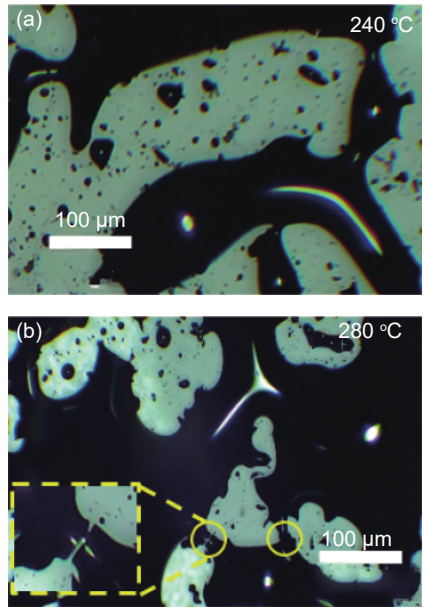

Fig. 7 The melting micrographs of (a) L-SP and (b) H-SP

facilitated easy elongation and the formation of uniform fibers.

H-SP contained more polar functional groups, increasing intermolecular interactions, thereby raising the viscosity of spinnable pitch. Furthermore, the larger PAHs in H-SP not only increased the average molecular weight but also facilitated stronger π-π stacking in the molten state, forming a rigid network structure that significantly increased melt viscosity and modulus. During spinning, melt swelling readily occurred[19], reducing fibers uniformity. L-SP featured smaller polycyclic aromatic hydrocarbon rings and longer alkyl side chains. These flexible side chains increased intermolecular free volume, weakened aromatic stacking forces, and reduced shear resistance[50]. Consequently, L-SP exhibited viscous-dominated behavior, ensuring continuous and stable spinning performance. As shown in the SEM images of pitch fibers (Fig. S8), the diameter of pitch fibers prepared by H-SP was uneven, fibers swelling occurred, while

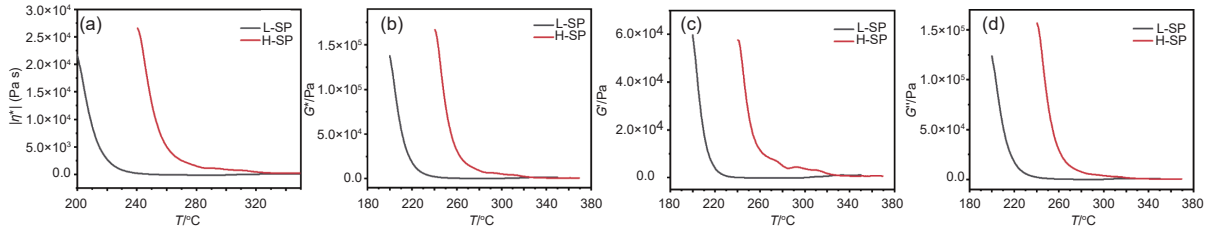

Fig. 8 The rheological properties of spinnable pitch, variation curves with temperature of (a) $|\eta^*|$, (b) G^*, (c) G', and (d) G''

the fibers formed by L-SP were more uniform.

The axial surface and cross-sectional images of CF-LSP and CF-HSP were shown in Fig. 9a–f. Both types of fibers exhibited a diameter of approximately 13–14 μm. The carbon fibers appeared uniform and dense, with no discernible voids or distinct skin-core structure. To quantify the surface heterogeneity, the gray-scale intensity profile analysis of the SEM images was used[51]. CF-HSP exhibited more pronounced fluctuations (Fig. S9). And the standard deviations of surface gray-scale distribution for L-SP and H-SP were 1.32 and 2.45, respectively, indicating poorer surface uniformity in CF-HSP. CF-HSP had blocky and granular protrusions, with particle sizes ranging from 1–5 μm, accompanied by wrinkled edges in the cross-section and internal inhomogeneity. CF-LSP contained fewer small particles, approximately 1–2 μm, with consistent diameter. The particles on the fiber surfaces likely originated from insoluble components within the spinnable pitch that could not be fully stretched and uniformly dispersed during spinning. Additionally, a high content of C=O and C=O−O groups was more prone to thermal decomposition, releasing CO and CO_2, which contributed to surface non-uniformity[52].

XRD patterns of resultant carbon fibers were shown in Fig. 10a. The resultant carbon fibers exhibited broad diffraction peaks near 24° (002) and 43° (100), suggesting disordered layered structures with randomly arranged carbon atoms. Compared with CF-LSP, CF-HSP showed the stronger peak intensity at 24° and similar peak intensity at 43°, indicating improved layer stacking in CF-HSP. Raman spectra were shown in Fig. 10b. The peaks D (1350 cm^{-1}) and G (1580 cm^{-1}) were associated with disordered structure and aromatic lamellar ordered structure[22]. I_G/I_D ratio was lower in CF-LSP (0.98) than in CF-HSP (1.00). CF-HSP exhibited higher local structural order. This analysis was consistent with the XRD results.

The tensile strength and modulus of CF-LSP were 731.95 MPa and 33.83 GPa, respectively, while those of CF-HSP were 762.75 MPa and 33.44 GPa (Fig. 10c). In general, CF-LSP and CF-HSP exhibited nearly comparable tensile strength and modulus. The performance characteristics of resultant carbon fibers were listed in Table S7. The coefficient of variation of tensile strength and modulus for CF-LSP was 5.84% and 3.86%. As for CF-HSP, it was 7.33% and 6.91%. The lower coefficient of variation and lower non-uniformity rate were shown in CF-LSP, demonstrating superior uniformity (Fig. 10c).

CF-HSP exhibited a more ordered microstructure, as confirmed by XRD and Raman analyses. In principle, such structural ordering should confer superior mechanical properties. However, this advantage was offset by its poor rheological behavior. Due to excessively high C=O content, H-SP exhibited a high-modulus melt at the spinning temperature, which readily led to melt swelling, reduced homogeneity, and non-uniform fiber diameters. Moreover, excessively high THFI content within the composition could not be uniformly stretched and dispersed, tending to

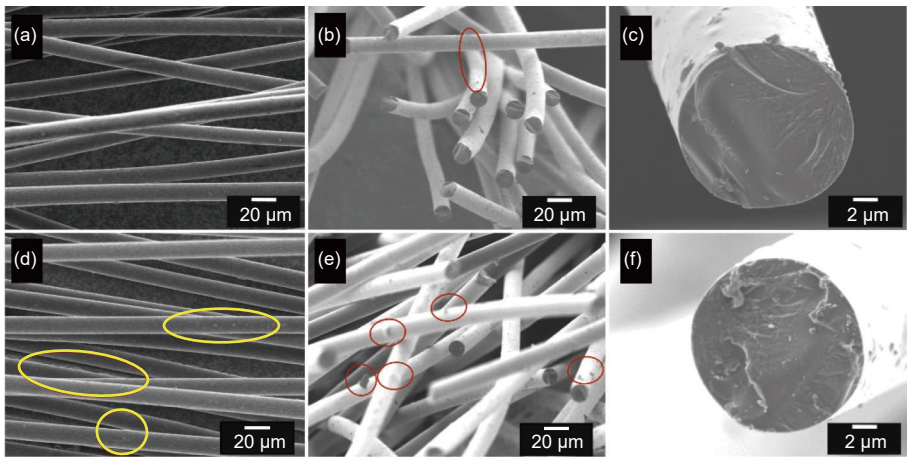

Fig. 9 SEM images of resultant carbon fibers: (a–c) CF-LSP and (d–f) CF-HSP

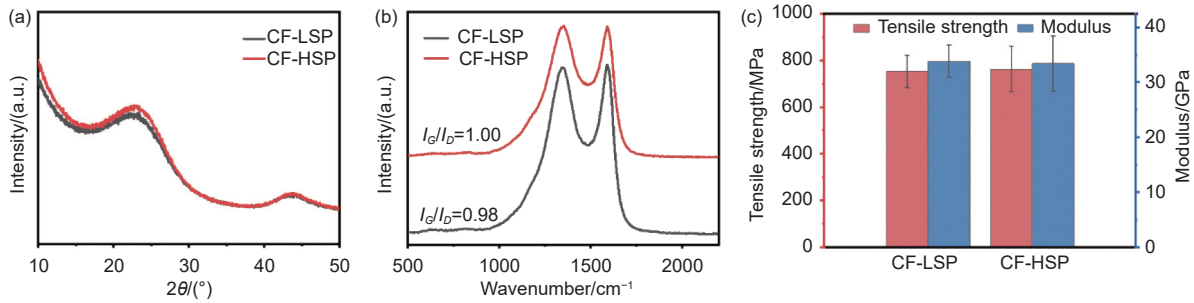

Fig. 10 (a) XRD patterns, (b) Raman spectra, and (c) the tensile strength and modulus of CF-LSP and CF-HSP

form aggregates within the melt and generate particles[21]. These particles and non-uniform regions within the fiber acted as stress concentration points under tension, leading to fiber fracture and diminishing its potential performance advantages. Conversely, although L-SP had a lower degree of condensation, its melt displayed viscous characteristics, enabling its performance potential to be maximized. The combined effects of the spinnable pitch structure and the particles and non-uniform property generated during processing resulted in similar performance for the resultant carbon fibers. Due to structural non-uniformity, the performance of CF-HSP exhibited poorer dispersion, with higher non-uniformity compared with CF-LSP. Therefore, the spinnable pitch should be prepared to possess a high aromatic hydrocarbon content, small PAHs size, and low C=O/O−C=O content. This provided it with superior structural characteristics and excellent viscoelastic properties, enabling uniform stretching, minimizing performance degradation caused by the production process.

4 Conclusion

This study elucidated the competitive interplay between molecular structural potential and rheological stability in determining the performance of pitch-based carbon fibers. H-SP exhibited a higher concentration of free radicals than L-SP, with a greater proportion of π-type oxygen-containing radicals and fewer aromatic hydrocarbon radicals. The number-average molecular weight increased from 864.86 Da (RCTP) to 1042.44 Da (L-SP) and 1662.84 Da (H-SP). L-SP had a lower polymerization degree, with longer alkyl side chains, and a higher proportion of C−O−C linkages. H-SP was characterized by larger polycyclic aromatic hydrocarbon structures, a higher degree of branching, as well as higher contents of C=O/O−C=O groups and THFI fraction.

In L-SP, the retained alkyl chains promoted intermolecular free mobility, creating a viscous-dominant melt. It promoted uniform stretching, maximizing the performance of carbon fibers (CF-LSP), compensating for structural disadvantages from its lower polymerization degree. Conversely, the high content of polar functional groups and large PAHs in H-SP induced strong intermolecular interactions and π-π stacking. At its spinning temperature, the molten H-SP exhibited a high modulus with balanced viscous and elastic properties, which made it prone to melt fracture and die swelling, resulting in surface particles and irregularities. Although CF-HSP exhibited superior performance potential, poor rheological properties led to surface inhomogeneity and particles. These acted as stress concentration points, making them prone to fracture during stretching, effectively diminishing the performance advantages derived from molecular order. Consequently, carbon fibers derived from two structurally distinct spinnable pitches exhibited comparable properties. CF-HSP exhibited a higher degree of non-uniformity than CF-LSP.

Therefore, regulating the proportion of oxygen-containing functional groups in spinnable pitch was crucial, not merely increasing molecular weight. Promoting the growth of PAHs while suppressing excessive polarity facilitated the maintenance of a favorable viscous property. This work provided a valuable reference for preparing high-quality spinnable pitch and

improving carbon fiber performance.

Declaration of competing interest

The authors declare that they have no known competing financial interests or personal relationships that could have appeared to influence the work reported in this paper.

Acknowledgements

This research was funded by Chinese Academy of Sciences Pilot Strategic Project A (XDA29050400), National Natural Science Foundation of China (U24A20548), National Natural Science Foundation of China (22479155), Innovation Fund of Institute of Coal Chemistry, Chinese Academy of Sciences (SCJC-XCL-2023-08), Open-end Fund Projects of China Institute for Radiation Protection Scientific Research Platform (CIRP2023OF001), Key Research and Development Projects of Shanxi Province (202101040201004), Shanxi Province PhD Project (2023SHB006).

References

[1] Zhu J D, Gao Z, Mao Q, et al. Advances in developing cost-effective carbon fibers by coupling multiscale modeling and experiments: A critical review[J]. Progress in Materials Science, 2024, 146: 101329.

[2] Yang J D, Li G, Gao L, et al. Effect of aromatization degree of mesophase pitch on cracks and mechanical properties of mesophase pitch-based carbon fibers[J]. Journal of Industrial and Engineering Chemistry, 2025, 142: 736-745.

[3] Gao H F, Lin X C, Zhang Y K, et al. Insight into the structural variation mechanism of highly spinnable isotropic pitch prepared by halogenated model aromatic compounds[J]. Journal of Analytical and Applied Pyrolysis, 2024, 180: 106541.

[4] You Z H, Xiao J, Wang G, et al. Molecular representation and atomic-level coking evolution investigation of modified coal tar pitch via ^{13}C NMR, MALDI-TOF-MS, SAXS, and ReaxFF MD[J]. Fuel, 2023, 348: 128561.

[5] Rani S, Kumar P, Kumari K, et al. Effect of carbonization conditions on microstructural properties of isotropic coal tar pitch-based general-purpose carbon fibers[J]. Diamond and Related Materials, 2023, 140: 110525.

[6] Sen K, Maiti A, Banerjee C, et al. Investigating the structure, dynamics, and phase behaviour of polycyclic aromatic hydrocarbons derived from coal tar pitch: (I) temperature dependence[J]. Journal of Molecular Liquids, 2024, 408: 125307.

[7] Vatsha M, Eterigho-Ikelegbe O, Bada S. A study of the efficacy and structural performance of modified coal tar and dimethylpolysiloxane as binders for coal-carbon composites[J]. Journal of Analytical and Applied Pyrolysis, 2024, 181: 106625.

[8] Liu J C, Shen C Y, Huang L J, et al. Preparation of pitch precursor with excellent spinnability for general-purpose carbon fibre using coal tar pitch as raw material[J]. Chinese Journal of Chemical Engineering, 2023, 54: 22-28.

[9] Rani S, Kumari K, Kumar P, et al. Isotropic coal tar pitch-based carbon fibers: effect of nitric acid towards elimination of air-stabilization step[J]. Journal of Industrial and Engineering Chemistry, 2023, 127: 283-294.

[10] Yang Y, Li Q, Zuo P P, et al. Investigation of the formation mechanism of mesophase pitch based on the evolution of molecular structure[J]. Fuel, 2026, 404: 136281.

[11] Liu J C, Liu Q, An X Y, et al. Mechanism and application of halogenation-dehalogenation in the development of pitch-based carbon fiber: A review[J]. Journal of Engineered Fibers and Fabrics, 2023, 18: 15589250231186945.

[12] Zuo P P, Fu S, He X Q, et al. Preparation of pitch-based carbon fiber from medium coal tar pitch refined by wash oil[J]. Fuel, 2025, 384: 133939.

[13] Saad S, Zeraati A S, Roy S, et al. Transformation of petroleum asphaltenes to carbon fibers[J]. Carbon, 2022, 190: 92-103.

[14] Chai L N, Yu E Q, Lou B, et al. Modification of isotropic pitch by tailoring chemical structure and fraction contents for enhancing carbon fiber mechanical properties[J]. Fuel Processing Technology, 2022, 233: 107290.

[15] Tian Y S, Ni Y, Dong Z J, et al. Synthesis of spinnable isotropic pitch from low-softening-point coal tar pitch via Blanc bromomethylation-dehydrobromination towards carbon fibers with enhanced mechanical properties[J]. Journal of Analytical and Applied Pyrolysis, 2024, 181: 106650.

[16] Tian Y S, Liu J A, Zhu H, et al. Co-carbonization of coal tar pitch and brominated industrial methylnaphthalene for the production of isotropic pitch-based carbon fibers with enhanced tensile strength[J]. Fuel Processing Technology, 2024, 255: 108058.

[17] Zuo P P, Qu S J, Shen W Z. Molecular growth from coal-based asphaltenes to spinnable pitch[J]. Materials Chemistry and Physics, 2022, 276: 125427.

[18] Zhai G G, Guo J G, Tian Y S, et al. Controllable preparation of spinnable isotropic pitches for carbon fibers with high tensile strength from low-cost ethylene tar pitch by a selective photobromination-debromination method[J]. Polymer, 2025, 316: 127862.

[19] Ye G M, Shi K, Wu H, et al. Improving the mechanical properties and thermal conductivity of mesophase-pitch-based carbon fibers by controlling the temperature in industrial spinning equipment[J]. New Carbon Materials, 2024, 39(2): 334-344.

[20] Tomaru T, Awakura Y, Kotajima M, et al. Effects of chemical structure of mesogenic components on the mechanical properties of mesophase pitch-based carbon fiber[J]. Carbon, 2025, 242: 120428.

[21] Li Q, Yang Y, Zuo P P, et al. Investigation of spinning performance based on the evolution of spinnable pitch components[J]. Journal of Analytical and Applied Pyrolysis, 2025, 192: 107310.

[22] Rani S, Kumari K, Kumar P, et al. Enhancing spinnability and properties of carbon fibers through modification of isotropic coal tar pitch precursor[J]. Journal of Analytical and Applied Pyrolysis, 2024, 181: 106566.

[23] Brünjes J, Seidel M, Dittmar T, et al. Natural asphalt seeps are potential sources for recalcitrant oceanic dissolved organic sulfur and dissolved black carbon[J]. Environmental Science & Technology, 2022, 56(12): 9092-9102.

[24] Podgorski D C, Walley J, Shields M P, et al. Dispersant-enhanced photodissolution of macondo crude oil: A molecular perspective[J]. Journal of Hazardous Materials, 2024, 461: 132558.

[25] Lambert T, Bouillon S, Darchambeau F, et al. Shift in the chemical composition of dissolved organic matter in the Congo River network[J]. Biogeosciences, 2016, 13(18): 5405-5420.

[26] Grunert B K, Tzortziou M, Neale P, et al. DOM degradation by light and microbes along the Yukon River-coastal ocean continuum[J]. Scientific Reports, 2021, 11(1): 10236.

[27] Amaral V, Romera-Castillo C, García-Delgado M, et al. Distribution of dissolved organic matter in estuaries of the southern Iberian Atlantic Basin: Sources, behavior and export to the coastal zone[J]. Marine Chemistry, 2020, 226: 103857.

[28] Amaral V, Romera-Castillo C, Forja J. Dissolved organic matter in the gulf of cadiz: Distribution and drivers of chromophoric and fluorescent properties[J]. Frontiers in Marine Science, 2020, 7: 126.

[29] Wasswa J, Driscoll C T, Zeng T. Contrasting impacts of photochemical and microbial processing on the photoreactivity of dissolved organic matter in an adirondack lake watershed[J]. Environmental Science & Technology, 2022, 56(3): 1688-1701.

[30] Groeneveld M, Catalán N, Attermeyer K, et al. Selective adsorption of terrestrial dissolved organic matter to inorganic surfaces along a boreal inland water continuum[J]. Journal of Geophysical Research-Biogeosciences, 2020, 125(3): e2019JG005236.

[31] Senesi N, Miano T M, Provenzano M R, et al. Characterization, differentiation, and classification of humic substances by fluorescence spectroscopy[J]. Soil Science, 1991, 152(4): 259-271.

[32] Cory R M, McKnight D M. Fluorescence spectroscopy reveals ubiquitous presence of oxidized and reduced quinones in dissolved organic matter[J]. Environmental Science & Technology, 2005, 39(21): 8142-8149.

[33] Yao H, Dai Q L, You Z P. Fourier transform infrared spectroscopy characterization of aging-related properties of original and nano-modified asphalt binders[J]. Construction and Building Materials, 2015, 101: 1078-1087.

[34] Zhu Y, Du C, Zheng H, et al. Molecular representation of coal-derived asphaltene based on high resolution mass spectrometry[J]. Arabian Journal of Chemistry, 2022, 15(1): 103531.

[35] Menéndez R, Blanco C, Santamaría R, et al. Effects of air-blowing on the molecular size and structure of coal-tar pitch components[J]. Energy & Fuels, 2002, 16(6): 1540-1549.

[36] Díaz C, Blanco C G. NMR: A powerful tool in the characterization of coal tar pitch[J]. Energy & Fuels, 2003, 17(4): 907-913.

[37] Blanco C, Santamaria R, Bermejo J, et al. A comparative study of air-blown and thermally treated coal-tar pitches[J]. Carbon, 2000, 38(4): 517-523.

[38] AlcanizMonge J, CazorlaAmoros D, LinaresSolano A, et al. Preparation of general purpose carbon fibers from coal tar pitches with low softening point[J]. Carbon, 1997, 35(8): 1079-1087.

[39] Yu B J, Wang C Y, Chen M M, et al. Two-step chemical conversion of coal tar pitch to isotropic spinnable pitch[J]. Fuel Processing Technology, 2012, 104: 155-159.

[40] Yao Q X, Liu Y Q, Tang X, et al. Multistage gradient extractive separation and direct and indirect analysis of petroleum ether insoluble fractions from low temperature coal tar[J]. Journal of Analytical and Applied Pyrolysis, 2022, 168: 105733.

[41] Fan X H, Li W, Chen L, et al. Sequential extraction of coal tar pitch and structural characterization of enriched large polycyclic aromatic hydrocarbons[J]. Chemistryselect, 2019, 4(17): 4874-4882.

[42] Xie L Y, Shao Y J, Zhong W Q, et al. Molecular dynamic simulation on the oxidation process of coal tar pitch[J]. Fuel, 2019, 242: 50-61.

[43] Cao D Y, Wang Z, Zhang G, et al. Regulating oxygen structure of coal liquefaction isotropic pitches to improve the mechanical properties of their general-purpose carbon fibers[J]. Journal of Analytical and Applied Pyrolysis, 2026, 193: 106541.

[44] Yamaguchi C, Mondori J, Matsumoto A, et al. Air-blowing reactions of pitch.1. Oxidation of aromatic hydrocarbons[J]. Carbon, 1995, 33 (2): 193-201.

[45] Liu J X, Jiang X M, Shen J, et al. Chemical properties of superfine pulverized coal particles. Part 1. Electron paramagnetic resonance analysis of free radical characteristics[J]. Advanced Powder Technology, 2014, 25(3): 916-925.

[46] Petrakis L, Grandy D W. Electron-spin resonance spectrometric study of free-radicals in coals[J]. Analytical Chemistry, 1978, 50(2): 303-308.

[47] Zhou B, Liu Q Y, Shi L, et al. Electron spin resonance studies of coals and coal conversion processes: a review[J]. Fuel Processing Technology, 2019, 188: 212-227.

[48] Graessley W W. Effect of long branches on the temperature-dependence of viscoelastic properties in polymer melts[J]. Macromolecules, 1982, 15(4): 1164-1167.

[49] Münstedt H. Rheological properties and molecular structure of polymer melts[J]. Soft Matter, 2011, 7(6): 2273-2283.

[50] Aho J, Boetker J P, Baldursdottir S, et al. Rheology as a tool for evaluation of melt processability of innovative dosage forms[J]. International Journal of Pharmaceutics, 2015, 494(2): 623-642.

[51] Croll S G, Payne S A. Quantifying abrasive-blasted surface roughness profiles using scanning electron microscopy[J]. Journal of Coatings Technology and Research, 2020, 17(5): 1231-1242.

[52] Niu H, Zuo P P, Shen W Z, et al. A comprehensive investigation on the chemical structure character of spinnable pitch for improving and optimizing the oxidative stabilization of coal tar pitch-based fiber[J]. Polymer, 2021, 224: 123737.